Imaging the complex geometry of a magma reservoir using FEM-based linear inverse modeling of InSAR data: application to Rabaul Caldera, Papua New Guinea

Erika Ronchin,[1,2] Timothy Masterlark,[3] John Dawson,[4] Steve Saunders[5] and Joan Martì Molist[1]

[1]*Group of Volcanology of Barcelona, Institute of Earth Sciences Jaume Almera, ICTJA-CSIC, Lluis Solé i Sabaris s/n,*
Barcelona E-08028, Spain. E-mail: erikaronchin@gmail.com
[2]*Mineralogy Petrology Tectonics Department of Earth Sciences, Uppsala University, Villavägen 16, SE-75236 Uppsala, Sweden*
[3]*Department of Geology and Geological Engineering, South Dakota School of Mines, Rapid City, SD 57701, USA*
[4]*Geodesy and Seismic Monitoring Group, Geoscience Australia, Cnr Jerrabomberra Ave and Hindmarsh Drive, Symonston, ACT 2609, Australia*
[5]*Rabaul Volcano Observatory, P.O. Box 386, Rabaul, East New Britain Province, Papua New Guinea*

SUMMARY

We test an innovative inversion scheme using Green's functions from an array of pressure sources embedded in finite-element method (FEM) models to image, without assuming an *a-priori* geometry, the composite and complex shape of a volcano deformation source. We invert interferometric synthetic aperture radar (InSAR) data to estimate the pressurization and shape of the magma reservoir of Rabaul caldera, Papua New Guinea. The results image the extended shallow magmatic system responsible for a broad and long-term subsidence of the caldera between 2007 February and 2010 December. Elastic FEM solutions are integrated into the regularized linear inversion of InSAR data of volcano surface displacements in order to obtain a 3-D image of the source of deformation. The Green's function matrix is constructed from a library of forward line-of-sight displacement solutions for a grid of cubic elementary deformation sources. Each source is sequentially generated by removing the corresponding cubic elements from a common meshed domain and simulating the injection of a fluid mass flux into the cavity, which results in a pressurization and volumetric change of the fluid-filled cavity. The use of a single mesh for the generation of all FEM models avoids the computationally expensive process of non-linear inversion and remeshing a variable geometry domain. Without assuming an *a-priori* source geometry other than the configuration of the 3-D grid that generates the library of Green's functions, the geodetic data dictate the geometry of the magma reservoir as a 3-D distribution of pressure (or flux of magma) within the source array. The inversion of InSAR data of Rabaul caldera shows a distribution of interconnected sources forming an amorphous, shallow magmatic system elongated under two opposite sides of the caldera. The marginal areas at the sides of the imaged magmatic system are the possible feeding reservoirs of the ongoing Tavurvur volcano eruption of andesitic products on the east side and of the past Vulcan volcano eruptions of more evolved materials on the west side. The interconnection and spatial distributions of sources correspond to the petrography of the volcanic products described in the literature and to the dynamics of the single and twin eruptions that characterize the caldera. The ability to image the complex geometry of deformation sources in both space and time can improve our ability to monitor active volcanoes, widen our understanding of the dynamics of active volcanic systems and improve the predictions of eruptions.

Key words: Inverse theory; Numerical approximations and analysis; Calderas; Remote sensing of volcanoes; Volcano monitoring.

1 INTRODUCTION

A significant challenge in assessments of volcano hazards is the accurate imaging of deformation sources, which represent magma migration and storage in both space and time. Our ability to predict future eruptions also relies on the knowledge of which parts of a reservoir are active versus those that could reactivate in the future due to magma migration through connected parts of a composite reservoir. Using customary simplistic *a-priori* deformation source geometries to represent these aspects strongly limits our explorations. The goals of this study, therefore, are (1) the introduction and testing of an innovative inversion that is based on finite-element method (FEM) models and that does not require an *a-priori* source geometry and (2) the application of this approach to the imaging of the extended shallow magmatic system responsible for the broad and long-term subsidence of Rabaul caldera. Mathematical models provide a link between the sources at depth (e.g. the deforming magmatic reservoir) and the observed system response at the surface. Parameters that describe the source (e.g. strength and geometric parameters) can be estimated, through inverse modeling, by comparing the observed natural system *response* (e.g. surface displacement) to the one predicted by a mathematical forward model of the *source*. The reliability of these models is customarily based on the goodness of predictions for a given set of available information, such as an interferometric synthetic aperture radar (InSAR) image.

Models with more complex source geometries generally allow the estimation of more parameters. This makes possible a more detailed investigation of real sources; however, at higher computational cost than simplified models. Therefore, subsurface processes of very complex volcanic systems are still interpreted on the basis of oversimplified sources that may ignore the complete assembly of available information. A consequence of this approximation is the estimation of a uniform, maximum pressurization of the magma reservoir which is incompatible with the rock strength. The pressurization can be reduced to more realistic values by claiming the effects of the inelasticity of the medium (e.g. Fernández *et al*. 2001; Trasatti *et al*. 2003; Hickey *et al.* 2015).

FEM models, referred to in the following as FEMs, allow us to take into account many realistic aspects of volcanic systems (e.g. topography and mechanical heterogeneities) which are difficult to represent with analytical models. However, the potential for the application of FEM models is restricted because of the use of computationally convenient source simplifications. Common simplifications of source geometry imply the use of *a-priori* and/or simplified source shapes. Based on geophysical studies, such as tomography, and geological field evidence, it is well known that magmatic reservoirs are generally geometrically complex (e.g. Smith *et al*. 2009; Burchardt *et al*. 2010, 2013; Jaxybulatov *et al*. 2014; Huang *et al*. 2015). This means that unrealistic aspects of the volcanic systems are introduced in the analysis by using models with simplified sources.

Using the principle of superposition of point sources embedded in elastic homogeneous half-spaces, a few studies attempted to simulate complex sources having arbitrary geometries (Vasco *et al.* 2002; Masterlark & Lu 2004). However, their results were limited by the simplification introduced when representing the complex heterogeneous nature of the volcanic edifice through an elastic homogeneous half-space. The goal of these studies was the characterization of the unknown source without using *a-priori* geometry, solving for the source strengths of an amorphous cluster of deformation sources distributed over a grid (e.g. Mossop & Segall 1999;

Vasco *et al*. 2002; Masterlark & Lu 2004; Camacho *et al*. 2011). This approach involves an array of simple sources, in which the source strengths are linearly related to the deformation via elastic equations. This allows the application of linear inverse methods. The assumption of linearity is common in volcano models, partly because the data may not constrain more complex rheology (Trasatti *et al.* 2008). Also, modeling inelastic behaviour requires much more computation.

Such a linear inversion based on an array of sources gives a geodetic image (Vasco *et al*. 2002) made of a distribution of source strengths that allows the identification of the position and the arbitrary shape of the reservoir. Presumably, this leads to a more realistic interpretation of deformational sources having complex geometry. This approach is generally applied to analytical models, for which the solutions used to build the Green's functions matrix are quickly and easily computed. The strategy is computationally challenging if applied to an inverse scheme based on FEMs, due to the fact that a new mesh of the domain needs to be generated for each source. Trasatti *et al*. (2008) overcame this problem by loading the faces of a cubic element of a meshed domain with three dipoles and three double couple forces, assembled in a stress tensor. However, their aim was to find depth, strength and ellipsoidal shape of a single pressurized source through the estimation of six elements of the stress tensor. If applied to the estimation of a grid of stress tensors, this source formulation would still generate a very expensive computational problem due to the high number of parameters to be estimated. Also, it needs to be justified by the quantity and the quality of available data sets (Trasatti *et al*. 2008). As a result, their investigation was limited to a single-source tensor.

We provide a computationally inexpensive strategy for the linear regularized least-squares inversion of InSAR data based on the Green's functions of an extended grid of FEM sources. The goal of the proposed inversion is to study the withdrawal of magma from a reservoir in order to define the amorphous shape and location of the unknown source in a volume previously constrained by the seismicity, geology and tomography. We apply our methodology to InSAR data of Rabaul caldera, Papua New Guinea, which recorded a broad long-term subsidence centred at the caldera between 2007 February and 2010 December. The volume within the FEMs that contains the magma reservoir of unknown shape is modeled with a grid of cubic sources, pressurized by the injection of magma mass, whose strength, implemented here as a mass flux of magma and resulting pressure change, is estimated during the inversion. This provides, through a source strength distribution, a more realistic image of the magma reservoir responsible for recent single and twin eruptions at the caldera.

2 RABAUL CALDERA DEFORMATION

Rabaul is a historically active collapse caldera with an elliptic shape having major and minor axes of 14 and 9 km, respectively, and outward dipping seismicity due to the elliptical fault zone located at the centre of the caldera (Fig. 1a). The volcanic activity is characterized by single eruptions (Tavurvur) at the eastern side of the caldera or twin eruptions (Tavurvur-Vulcan) at opposite sides of the caldera.

Analytical models of Rabaul caldera displacements, which occurred during the deformational crisis of 1983–1985 and the period prior to the twin eruptions of 1994 (which culminated in a plinian eruption of Vulcan), estimated a shallow source (between 1.2 and 2 km depth) southeast of Matupit Island, under Greet Harbor (McKee *et al*. 1984, 1989; Archbold *et al*. 1988), and a deeper
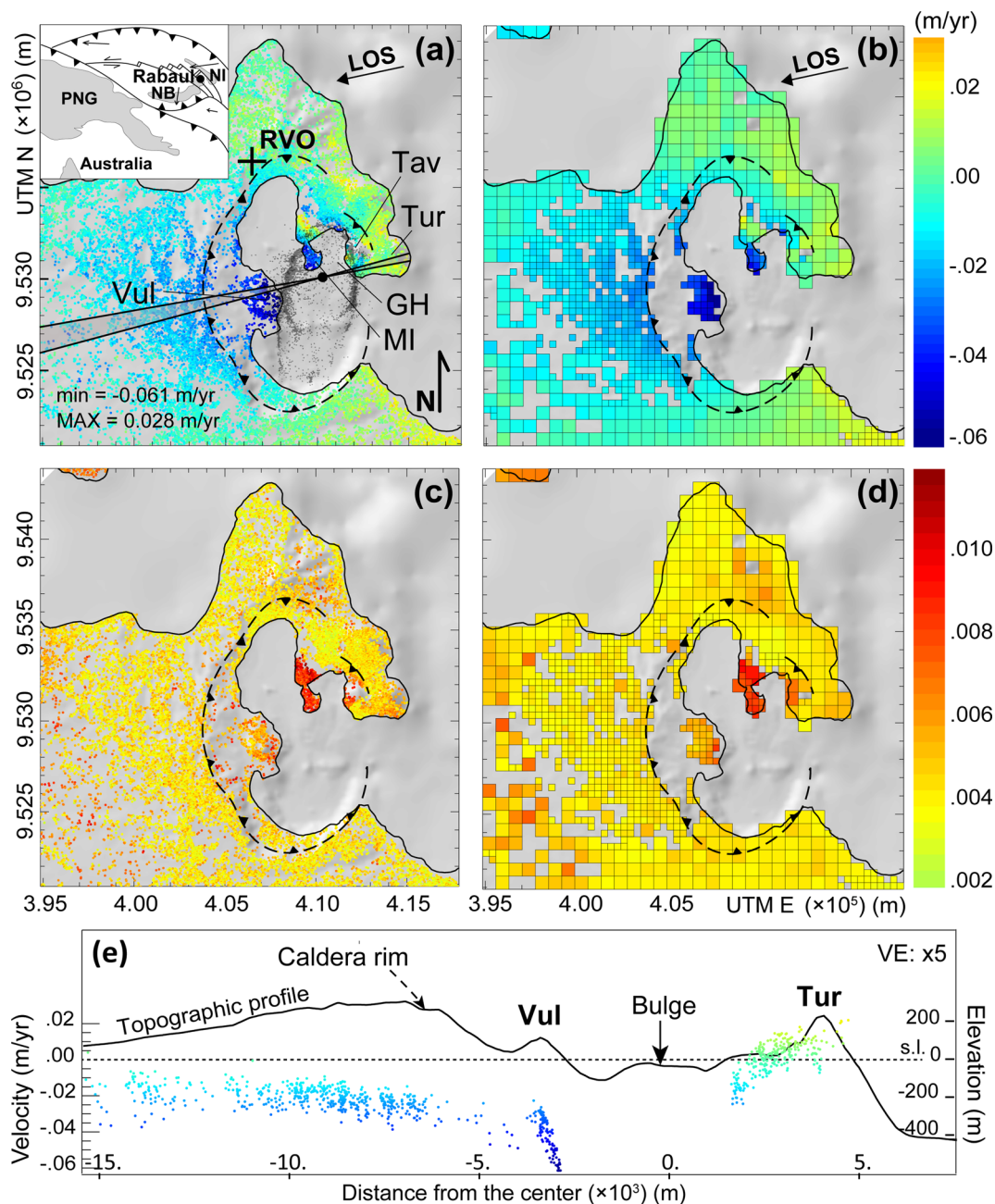
Figure 1. Persistent scatterers (PS) mean LOS velocities of 20 ALOS-PALSAR ascending images acquired between 2007 February 27 and 2010 December 8. (a) Mean LOS velocities. The black arrow on the top-right corner represents the projection of the LOS on the surface (direction towards the satellite). Caldera rim (barbed dashed lines), Greet Harbor (GH), Matupit Island (MI), Turanguna (Tur), Tavurvur (Tav) and Vulcan (Vul) edifices. Elliptical distribution of the seismicity in dark grey dots (from Saunders 2001). Inset: location map showing Papua New Guinea (PNG), New Britain island (NB) and New Ireland island (NI). (b) Quadtree subsampling of mean PS-InSAR velocity. (c) Standard deviation of mean LOS velocity and (d) corresponding values for the quadtree subsampling. (e) LOS velocities (dots with colours as in panels a and b) of sectors (shaded sectors in panel a) and topographic profile at radial distance from the possible source (black dot in panel a).

source near Vulcan at 3 km depth (McKee *et al*. 1984). FEMs have been used to explain the deformation prior to the 1994 twin eruptions with the interaction between an expanding reservoir and the elliptical faults (De Natale & Pingue 1993; De Natale *et al*. 1997; Ronchin *et al*. 2013) or the migration of fluids into the elliptical faults (Saunders 2001). To the authors' knowledge, no FEMs have been constructed to understand the recent deformation and the actual shallow magmatic system that feeds frequent and important eruptions at Rabaul caldera.

In 2006 October, Tavurvur erupted >0.2 km³ of andesite with a subplinian eruption (Saunders *et al*. 2007). A period of quiescence followed, with no surface deformation. From 2007 February, the activity of Rabaul caldera area was characterized by almost continuous Tavurvur vulcanian eruptions and by the deformation modeled in this work: a general long-term subsidence of a broad area centred at the caldera and detected by InSAR data between 2007 February and 2010 December. During this period, no changes of products composition were observed (Rabaul Volcano Observatory (RVO) reports in

Table 1. Summary of ALOS-PALSAR images and parameters used for the data reduction.

Aspect	Specifications
InSAR data	
20 images	From 2007 February 27 to 2010 December 10
Total days	1380
Wavelength (m)	0.236 (L-band)
Pass	Ascending
Track	352
Frame	7090
Heading (centre of the swath) (°)	−12.06
Incidence (centre of the swath) (°)	37.8
LOS (line of sight) [east, north, up]	[−0.617, − 0.131, 0.775]
Pixel dimensions (m × m)	Nominal pixel size is 4.7 × 3.5 (range × azimuth)
Area covered by scenes (km^2)	70
Number of coherent pixels	55 148
Rabaul study area (km^2)	23
Number of coherent pixels of Rabaul area	22 123
Reduced data	
Maximum size of quadrants (m)	1000
Minimum size of quadrants (m)	300
Minimum number of PS in the quadrant	5
Variance threshold (m^2 yr^{-1})	0.0001
Threshold of the mean index of strength and stability^a	3.5
Number of reduced quadrants	802

[a]See the Supporting Information for definitions.

Smithsonian Institution 2013), suggesting a phase of a semi-open system characterized by magma withdrawal with no new magma input from deeper reservoirs.

2.1 Rabaul InSAR data

We employed 20 PALSAR images acquired by the ALOS satellite of the Japanese Space Agency (JAXA) between 2007 February 27 and 2010 December 8 (information summarized in Table 1). We processed the ALOS raw data using the ROI_PAC software developed by JPL/Caltech (Rosen *et al*. 2004). We formed the interferograms using the Doris software developed by the Delft University of Technology with respect to a master image (see Supporting Information, Fig. S3), chosen to minimize perpendicular and temporal baselines. Unlike conventional InSAR analysis, no azimuth and range spectral filtering was undertaken to maintain the resolution (Hooper *et al*. 2007). The topographic signal was estimated using the 3 arcsec digital elevation model from the Shuttle Radar Topography Mission (SRTM, Farr *et al*. 2007).

A time-series analysis of the interferograms was then undertaken using the persistent scatterers (PS) InSAR approach implemented in the StaMPS software (Hooper *et al*. 2007) (percent_rand and clap_win set to 20 and 32, respectively). The PSInSAR technique has been used to overcome many of the problems associated with decorrelation observed in conventional InSAR techniques by identifying pixels which remain coherent (phase stable) over long periods of time (Hooper *et al*. 2007). A major advantage of the PSInSAR method for studies of volcanoes is that no *a-priori* functional model of the temporal deformation is required, since the method relies on an assumption that any deformation signal is spatially correlated. Deformation was estimated simultaneously with nuisance parameters, including atmospheric and residual topography signals, where the signal components were separated by exploiting their temporal and spatial characteristics. Phase unwrapping was performed using the 3-D approach of Hooper & Zebker (2007) (for time-series, see

Supporting Information, Fig. S3). Line of sight (LOS) mean velocities were estimated with respect to a manually selected area of pixels outside the area of active deformation. The uncertainty (1σ) of the velocities was estimated as ±1 cm yr^{-1} and determined from an analysis of the individual time slices of pixels outside the area of deformation.

Because one goal of this study is the understanding of the extended shallow magmatic system responsible for the broad and long-term subsidence, we investigate the LOS mean velocities over the entire time period of SAR acquisition (Fig. 1a), assuming that this period is long enough to record the response of the entire magma reservoir to a long, almost continuous magma withdrawal due to the Tavurvur eruptions.

A wide area, including the caldera and an area west of the caldera, shows relative negative LOS velocities, with highest values of −60 mm yr^{-1} between the southwestern tip of Matupit Island and Vulcan's northeastern side (Fig. 1a). Positive LOS displacements are recorded in the eastern areas outside the caldera border. Standard deviations (SD) associated with the mean LOS velocities show the deviation from a linear steady subsidence over the study period (Fig. 1c). High SD for Matupit Island identify strong nonlinear motion of PS, possibly related to the most shallow processes (e.g. impulses of magma ascent to the surface or hydrothermal processes). The highest SD, along the southwestern side of the old airport strip, are associated with a localized area of anomalous positive LOS velocities suspected to be related to hydrological processes, since this is a drainage area.

The unwrapped InSAR image contains approximately 22 × 10^3 PS (Fig. 1a). In order to accommodate computational requirements of the modeling, we reduced the number of pixels using a variance quadtree algorithm (Samet 1990; Lohman & Simons 2005; Minasny *et al*. 2007) that spatially subsamples the interferogram (see Supporting Information). With this procedure, we reduced the number of data by about two orders of magnitude (Table 1) without losing important information (Figs 1b and d).
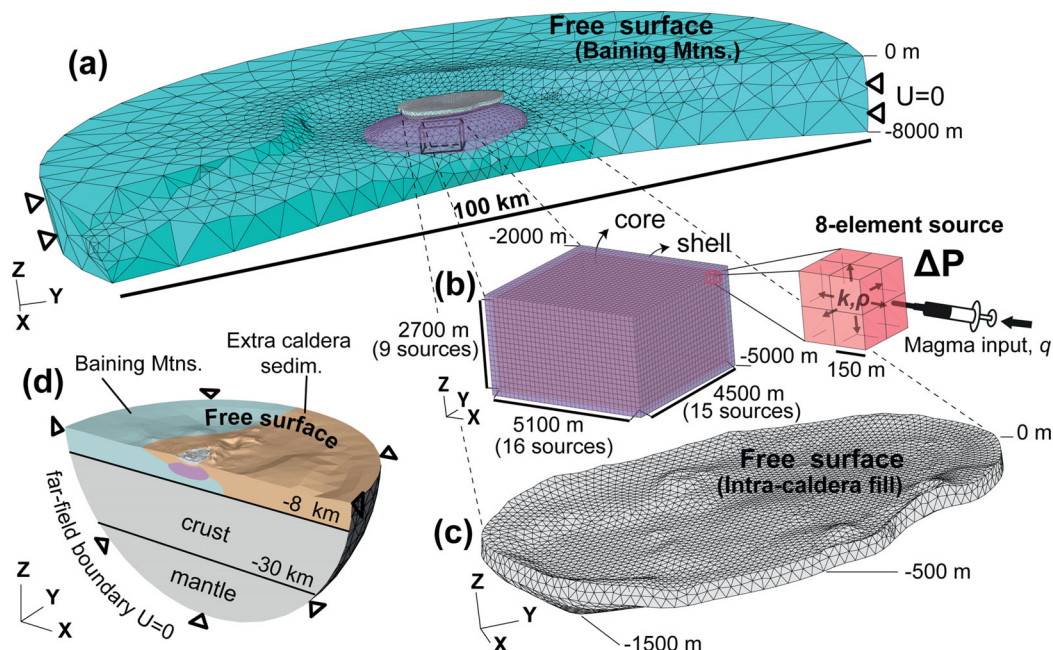
Figure 2. Assembling the 3-D Rabaul caldera model (modified from fig. 4 of Ronchin *et al.* 2013). (a)–(c) Blocks of the upper 8 km. Colours indicate different material properties summarized in Table 2. (a) Baining Mountains block (sky blue), intrusive block (purple) and intracaldera fill block (light grey). The extra-caldera deposits block has been removed to permit the visualization of inner blocks. Hollow triangles represent pinned boundaries. (b) Central prism meshed with hexahedral elements: core hosting the cubic sources and the shell around it. (c) Intracaldera fill block. (d) Material properties distribution and boundary conditions of the FEM domains.

A profile through the InSAR data (Fig. 1e) shows the most important features of the signal: a broad region of negative LOS velocities outside the caldera, a high-velocity gradient above the Vulcan edifice, loss of data in the area occupied by water and positive LOS velocities above Turanguna and the southern part of Tavurvur.

Neither the seismicity recorded (RVO reports in Smithsonian Institution 2013), nor the distribution of InSAR velocities, suggests movement along the outward dipping elliptical faults during the study period. This encourages us to investigate an extended subsurface magma withdrawal from the shallow reservoir as a possible source of deformation.

3 METHOD: LINEAR INVERSION BASED ON FEMs, USING RABAUL CALDERA AS AN EXAMPLE

Inspired by the source cluster method consisting of a relatively dense 3-D array of analytical point sources (Vasco *et al.* 2002; Masterlark & Lu 2004; Battaglia & Vasco 2006; Camacho *et al.* 2007, 2011), we model a volume of the Rabaul FEM model domain with a prism of cubic hexahedral elements (Abaqus 2009) that serves to generate a regular 3-D array of elementary sources (Fig. 2b). These are generated one at a time by removing elements of the prism and pressurizing the resultant cavities by injecting a fluid flux. The collection of all source solutions generates a library of pre-computed elementary solutions on the basis of the Green's functions matrix used to solve the inverse problem. The fluid flux and related pressurization in each cavity are estimated through linear inversion. This way, rather than imposing an *a-priori* source geometry, we can assume that the source of deformation is represented by a subset of the array of sources with an amorphous shape dictated by the data. The use of FEMs for this process allows us to

simultaneously account for the arbitrary geometric configurations and the distributions of elastic properties.

3.1 FEMs configuration and deformation sources

New FEMs for Rabaul caldera (Fig. 2) are built by implementing a model having heterogeneous distribution of elastic materials (Ronchin *et al.* 2013). The models are implemented with a discretization of the prismatic volume (Fig. 2b) containing the reservoir.

Due to the need of satisfying both low-velocity tomographic contrast interpreted as a shallow reservoir (Finlayson *et al.* 2003) and the hypocentres' location (Mori & McKee 1987; Jones & Stewart 1997; Saunders 2001), the chosen prismatic volume hosting the FEM sources at the centre of the caldera (i.e. pressurized cavities) occupies most of the low-velocity zone imaged by the tomography (Fig. 3c) and laterally encloses the hypocentres (Figs 3a and b). Keeping in mind that no shear is possible in fluids, and thus considering the hypocentres as lateral boundaries for the magma storage zone in the upper part of the reservoir, we estimate that the central prism hosts the unknown reservoir in a conservative way, although it does not entirely occupy the lateral extension of low seismicity (Fig. 3c). The prism is confined between 2000 and 5000 m depth and thus is fully included in the intrusive block. The deeper side of the prism is far below the deeper hypocentres recorded along the elliptical faults and below the bottom of the shallow reservoir imaged by the tomography (Finlayson *et al.* 2003), ensuring the investigation of a shallow magma reservoir constrained by the geophysical studies (Fig. 3).

A complete description of an FEM model includes the governing equations, initial conditions, boundary conditions, applied loads and the tessellated geometric domain. The 3-D problem domain approximates a solid hemisphere with a diameter of 100 km
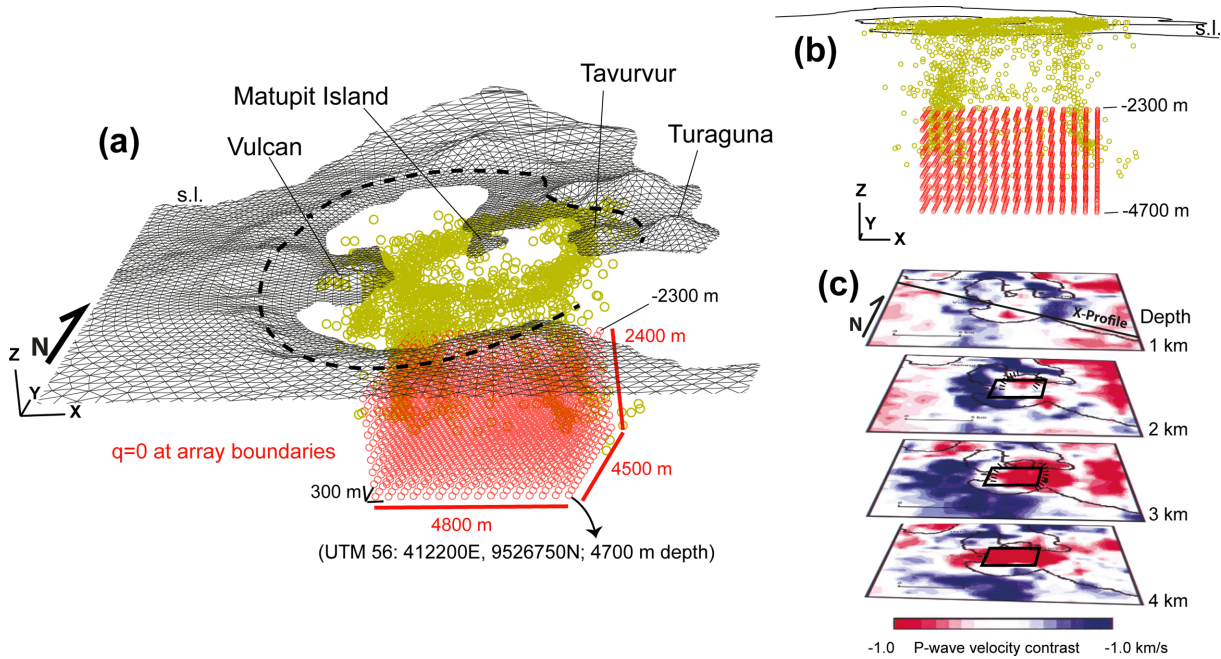
Figure 3. Extension of array of sources. (a) Centroids of FEM cubic sources (red circles) with respect to the seismicity (yellow circles, hypocentres and epicentres digitalized from Saunders 2001). The dashed black line indicates the border of the caldera. Free-surface mesh under sea level (s.l.) is omitted for clarity. (b) North view. (c) Velocity contrast slices at 1, 2, 3 and 4 km depths under the central Rabaul caldera adapted from fig. 11 of Finlayson *et al.* (2003). Dashed lines on the slices at 2 and 3 km represent the seismically active portions of the ring fault above 2 km and below 3 km, respectively. Black frames represent the footprints of source array.

Table 2. FEM configuration and parameters.

Aspect	Specifications		
Domain extension (m)	(UTM zone 56 M)		
	$X_{\min}$ = Easting 3.6048e+05		
	$X_{\max}$ = Easting 4.6048e+05		
	$Y_{\min}$ = Northing 94.8075e+05		
	$Y_{\max}$ = Northing 95.8078e+05		
Centre of domain (m)	$x = 4.1052e$+05, $y = 95.3091e$+05		
Analysis type	Elastic		
Domain radius (m)	50e+03		
Max domain depth (m)	50e+03		
Far-field boundary conditions	Zero displacement		
Top of problem domain	Topographic relief		
Mesh			
Part-1 domain	141 834 first-order tetrahedral elements		
Part-2 central prism core	17 280 first-order hexahedral elements		
Part-2 central prism shell	4480 first-order hexahedral elements		
Geological block	Volume (m^3)	Young's modulus, E (Pa)	Poisson's ratio, υ
Intracaldera fill[a]	6.61×10^{10}	0.20×10^9	0.15
Extra caldera[a]	2.48×10^{13}	4.08×10^9	0.28
Baining Mountains [a]	3.69×10^{13}	47.86×10^9	0.28
Intrusive complex[a]	5.48×10^{11}	56.45×10^9	0.29
Crust (oceanic crust)[b]	1.45×10^{14}	100.00×10^9	0.25
Mantle[c]	5.46×10^{13}	174.59×10^9	0.28
Magma	Density (kg m^{-3})	Bulk modulus, k (Pa)	
Andesitic magma[d]	2370.00	4.50×10^9	

[a]Material properties scaled to static values. See the Supporting Information.
[b]Elastic properties from Got *et al.* (2008).
[c]Elastic properties from Turcotte & Shubert (2002).
[d]Average properties calculated using Huppert & Woods (2002) formulae. See the Supporting Information.

centred on the caldera, whose upper surface is a stress-free surface represented by the topographic and bathymetric relief. The FEMs configuration is summarized in Table 2. At the outer surface of the hemisphere, far enough from the caldera for displacements

to vanish, we specified zero displacements (Figs 2a and d). The governing equations describe elastic behaviour in a 3-D domain having no body forces and a spatial distribution of isotropic elastic material properties E (Young's modulus) and σ (Poisson's ratio).

The FEM formulation assumes infinitesimal (quasi-static) elastic strain.

The FEM domains are formed by two parts: (1) a heterogeneous part made of six geological blocks with a shape and size described in Ronchin *et al*. (2013) and defined by tomography and geology (Figs 2a, c and d), and (2) a central prism surrounded by the intrusive block (purple body in Figs 3a and b), both of them having the same material properties. The bulk dynamic elastic properties of the geological blocks (Table 2) are calculated from the *Vp* velocities provided by the tomography (Finlayson *et al*. 2003) and scaled to static values (see Supporting Information for further information). The equivalence between dynamic and static elastic properties is valid for depths greater than a few kilometres (Simmons & Brace 1965). The central prism is meshed with cubic elements (150 m edge length) that ensure the generation of a regular array of sources. The surrounding domain is entirely partitioned with tetrahedral elements, due to their ability to assume complex shapes (e.g. topography). On the free surface, the characteristic length of the tetrahedral element edges is about 200 m for the elements above the prism containing the sources, where a higher displacement gradient is expected, and gradually increases up to about 3000 m near the far-field boundary, where lower displacement gradients are expected. Continuity of displacements between the two different meshes of the two parts is guaranteed by coupling the displacements of element nodes along the sides of the central prism where the two parts have the same number of nodes at the same position, thus forming pairs of nodes (see Supporting Information). The central prism (Fig. 2b) is made of (1) a core from which elements are removed to generate the array of pressurized sources and (2) a shell of cubic elements not used for the source generation. Multiple FEMs, each having a different *i*th pressurized cavity (300 m edge dimension), are sequentially generated by removing a different group of eight elements (150 m edge dimension) from the core of the common FEM model mesh (Fig. 2b). Elements of the core not removed at the time of the *i*th source generation are part of non-active sources and are structural elements having material properties of the intrusive block in which they are included. Duplicate material properties characterize the elements of the shell that are not used to generate the cavities (Fig. 2b). Their role is to guarantee a smooth transition between the cubic sources and the tetrahedral mesh, and a uniform discretization of the volume around all sources. This ensures that all the sources equally behave as a centre of dilatation (i.e. McTigue finite source) (see the Supporting Information, Figs S1 and S2). All eight elements chosen to generate the *i*th cavity are removed only once. This means that a virtual regular array of non-overlapping cavities is formed and that we obtain 2160 cavities arranged in nine vertical layers (Figs 2b, 3a and b) from a total of 17 280 cubic elements constituting the core.

Initially, each elementary cavity is generated and filled with a compressible hydraulic fluid (i.e. magma having bulk modulus *k* and initial density, pressure and volume) by: (1) removing eight elements from the central prism to form an *i*th cubic cavity and (2) coating the cavity with Abaqus volumetric hydrostatic fluid elements (Abaqus 2009), which fill the cavity with a mass of magma in equilibrium. The source of deformation is then initiated by injecting a fluid load *q* (in kg) into the filled cavity through the hydrostatic fluid elements. In response to *q*, the current hydrostatic fluid pressure P_c is given via the equation:

$$P_c = -k\rho \left(\rho_c^{-1} - \rho_{in}^{-1} \right) \tag{1}$$

where ρ is the reference density of the fluid at zero pressure, ρ_{in} is the initial density of fluid filling the cavity (where $\rho_{in} = \rho$, if no temperature dependency of the fluid is considered) and ρ_c is the fluid density at current pressure. The process is isothermal and *k* is independent of change temperature. Properties of the fluid (i.e. magma of Rabaul reservoir) used for the computation of the Green's functions are summarized in Table 2 (see the Supporting Information for further information). By removing the elements from a common prism, we do not have to remesh the model in order to generate new sources, thus saving time and computational resources. The final isotropic pressure change ΔP_i, as well as the volume change ΔV_i of the *i*th cavity of the array, are solutions variables computed in response to: (1) the fluid mass q_i injected through the hydrostatic fluid elements (Abaqus 2009) and (2) the accommodation of the cavity structure. ΔP_i is thus numerically calculated by Abaqus in terms of fluid bulk modulus, cavity geometry and the material properties surrounding the cavity. The hydrostatic fluid elements, besides allowing the injection of the fluid mass, provide the coupling between the deformation of the cavity and the change in pressure, ΔP_i. We have verified that at the pressure range, cavity geometry and material properties considered, ΔP_i is linearly related to q_i. By this definition, we assume that the change of pressure is entirely and only due to a concordant change of mass in the source, the flux of magma.

## 3.2 Linear inversion based on a family of FEMs

We generate a family of multiple FEMs whose different cavities are non-overlapping, equal volume and distributed in a regular array. This array of sources allows a relatively simple finite-difference formulation of the Laplacian smoothing operator **L**, to regularize the solution of the linear inverse problem. Each cavity of the array is loaded with a unit mass of magma of 1×10^9 kg in order to generate one pressurized source in each FEM model of the family, whose strength will be estimated during the inversion. The fact that the prism is bigger than the possible reservoir allows us to account for the boundary conditions applied to the array of sources during the inversion process and to limit the effects of the boundaries. We assume no sources outside the 3-D array and apply Dirichlet-type boundary conditions (Wang & Anderson 1982; Fig. 3a). The linear relationship with the induced displacements is validated by performing an FEM-based linear inversion of Rabaul synthetic data, provided in Fig. S4 in the Supporting Information.

The forward solution for the displacements at the free surface, caused by the array of expanding FEM cavities, is the superposition of the displacements generated by each of the sources. To determine the 3-D distribution of change of pressure and the flux of magma entering or leaving the sources of the array, we estimate the elements of a vector **q** through a weighted least-squares inversion to solve the equation:

$$\begin{pmatrix} \mathbf{WG} & \mathbf{xy1} \\ \beta\mathbf{L} & \mathbf{000} \end{pmatrix} \begin{pmatrix} \mathbf{q} \\ a \\ b \\ c \end{pmatrix} = \begin{pmatrix} \mathbf{Wd} \\ \mathbf{0} \end{pmatrix} \tag{2}$$

where **G** is a 802 by 2160 matrix of Green's functions (displacements generated by the overpressure due to the injection of a unit mass of magma, 1×10^9 kg, into each FEM source of the array and projected onto the LOS), **d** is the vector of observed LOS displacements, **W** is a diagonal matrix of data weights whose $W_{i,i}$ element is the reciprocal of the variance σ_i of the *i*th datum d_i and **L** is the finite-difference approximation of the Laplacian smoothing operator (Freymueller *et al*. 1994), whose construction is extensively described by Masterlark & Lu (2004). By weighting the data with the corresponding SD (Fig. 1d) through **W**, we give higher influence
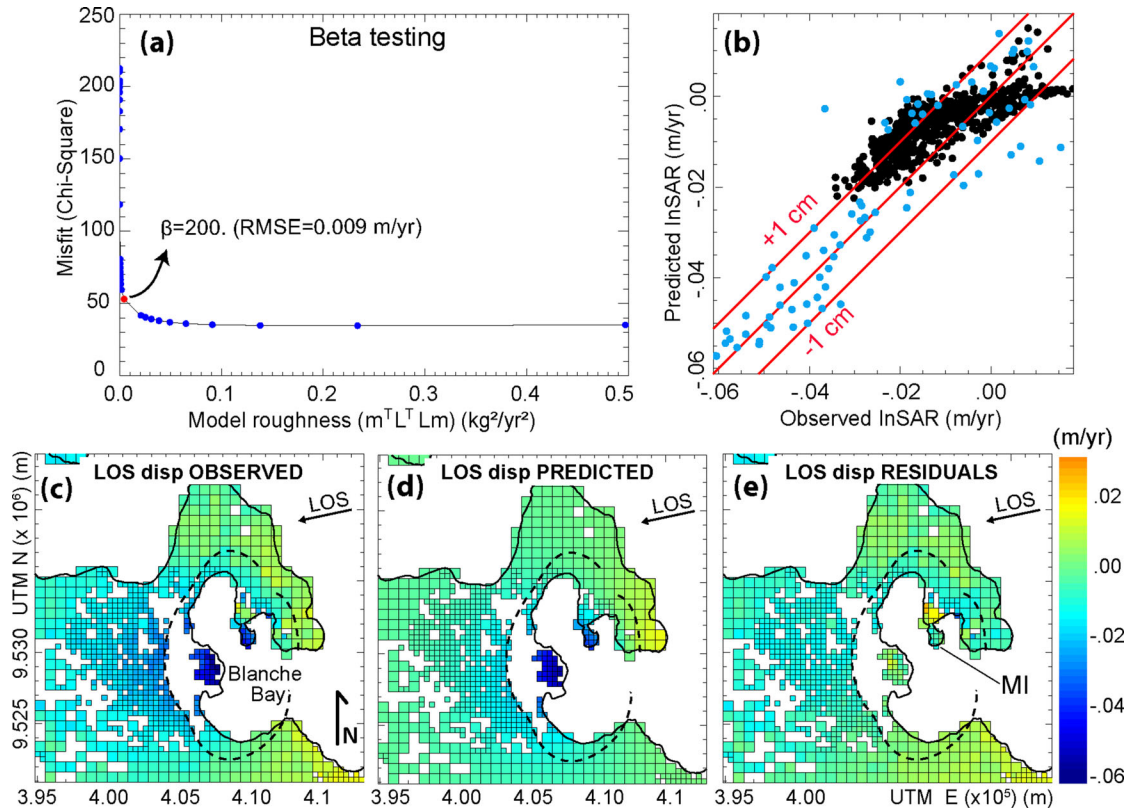
Figure 4. InSAR data inversion. (a) Model misfit versus roughness. The L-curve gives the trade-off between the chi-square values (between the observed and the predicted displacements) and model roughness. The preferred solution for β-value is at the knee of the L-curve (red dot). (b) Observed versus predicted LOS displacements. Blue and black dots represent displacements at positions inside and outside the caldera, respectively. The two red lines, located at $+1$ and -1 cm from the diagonal line of perfect predictions, identify a buffer zone that represents the accuracy of the InSAR. (c) Observed and (d) predicted LOS displacements. (e) Residuals: observed–predicted LOS displacements. Matupit Island (MI).

to the data with steady LOS displacements (assumed to be related to the overall deflation of the entire reservoir, the target of the study). The importance of **L** is governed by the size of a scalar damping parameter β that controls the relative importance of minimizing the roughness of the solution versus fitting the data. **L** is defined in a way that allows: (1) the application of Dirichlet-type boundary conditions (Wang & Anderson 1982) to **q** along the outer boundaries of the source array (Fig. 3a) and (2) the assumption of no sources outside the source array. The phase ramping in the InSAR image, caused by the uncertainties of the satellite position (Massonnet & Feigl 1998), is taken into account in eq. (2) by simultaneously fitting a plane. To do so, **G** is appended with three column vectors **xy1** corresponding to the position of the InSAR data (**x** and **y**) and a unit vector. The unknown linear parameters for the vertical projection of the plane (a, b and c) are appended to **q**.

The value of the damping parameter β that weights the smoothing operator is determined from the trade-off analysis between the misfit of the predicted displacements with respect to the observed displacements and the roughness of the inversion solution defined by $\|\mathbf{Lm}\|_2^2 = \mathbf{m}^\mathsf{T}\mathbf{L}^\mathsf{T}\mathbf{Lm}$. Note that the weighted smoothing appends the weighted **G** matrix. The three null column vectors [**000**] are necessary to preserve the matrix dimensions associated with the nuisance parameters [**xy1**]. By performing the inversion using the value of β at the knee of the curve (Fig. 4a), we identify a weighted least-squares damped (WLSD) inversion for solutions that is a good compromise between fitting the data versus minimizing the solution roughness (i.e. complexity of the model) and satisfying the boundary conditions.

In order to obtain the model solution for the distribution of mass change (i.e. the flux of the fluid magma) in the array during the time frame of data acquisition, the estimates of the sources' strength **q** are scaled by the unit mass of injected magma. For each ith source, the change in pressure ΔP_i, being linearly correlated to the corresponding injected fluid mass, can be calculated by scaling the FEM solution for the unit hydrostatic change in pressure P_i by the correspondent source strength estimate q_i:

$$\Delta P_i = P_i q_i. \tag{3}$$

Model estimates are fully described by providing their uncertainties and the model resolution, essential to interpreting models in terms of reliability (Aster *et al.* 2005). In this work, the model resolution is provided through a checkerboard test. Its aim is to show how well the estimated source parameters are independently resolved and how significantly smoothed or otherwise biased our solution compares to the true (but unknown) solution.

The uncertainties associated with model estimates depend on the covariance of the data and on the way errors are mapped from the data to the model parameters. They are described by the diagonal elements of the model covariance matrix (Menke 1989):

$$\boldsymbol{C}_m = \left(\hat{\mathbf{G}}^T \hat{\mathbf{G}}\right)^{-1}. \tag{4}$$

where $\hat{\mathbf{G}}$ is the first bracketed term on the left side of eq. (2).
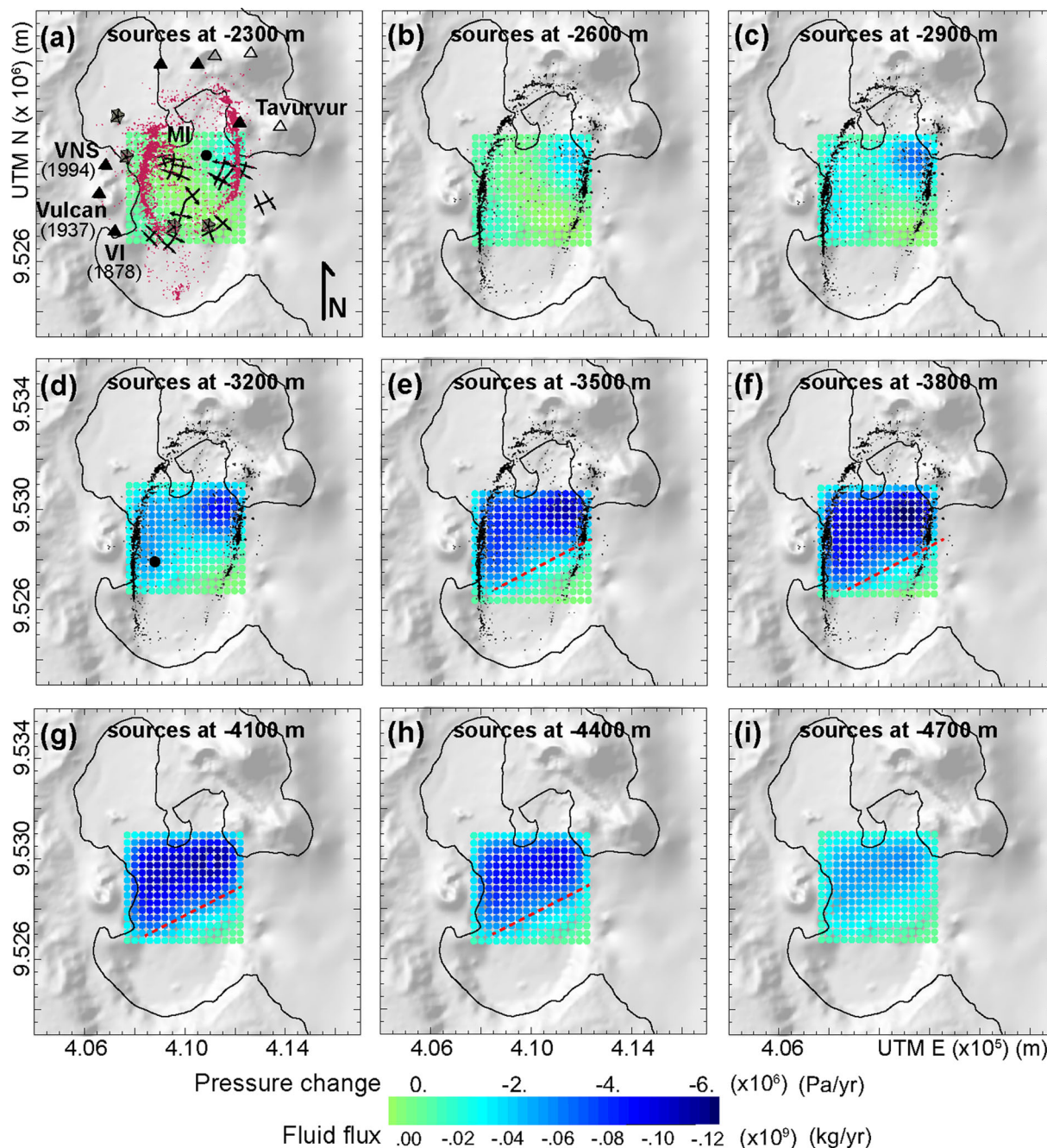
Figure 5. Distributed flux of fluid and pressure changes among the source array. (a)–(i) Solutions of the FEM-based normalized inversion at different depths. The solutions represent the flux of fluid (or change in pressure) at each source of the array. Blue values represent a negative flux (i.e. mass of fluid flowing out of the source). Black filled circles (in panels a and d) stand for inflation centres proposed by McKee *et al.* (1984). (a) MI—Matupit Island, VNS—Vulcan North Shore and VI—Vulcan Island. Black triangles for post-caldera cones, hollow triangles for pre-caldera cones. Folds mapped by seismic reflection surveys (Pono 1990). Grey stars for submarine cones. Shallow hypocentres (<2 km) are marked with red dots (from Saunders 2001). (b)–(f) Deeper seismicity (between 2 km and about 3.8 km depth) is marked with black dots (from Saunders 2001).

4 RESULTS: DISTRIBUTED SOURCES AND THE 3-D GEOMETRY OF THE RABAUL SHALLOW RESERVOIR

The strength distribution of sources in the array (Figs 5a–i) is estimated in terms of both fluid flux and related pressure changes from the reduced InSAR data through a linear least-squares inversion (eqs 2 and 3), sweeping through a range of damping values of β. The result is an L-curve of points at the knee of which the preferred solution is visually identified (Fig. 4a). The preferred

damping value, $\beta = 200$, corresponds to a root mean square error (RMSE) of 0.0091 m yr^{-1} and is chosen in a way that the data are neither substantially overfit, nor underfit with respect to the estimated data errors. This misfit, being of the same order of magnitude as the roughly estimated accuracy of the InSAR data (0.01 m yr^{-1}) used for the inversion, is acceptable. The comparison of observed versus estimated LOS displacements (Fig. 4b) shows a diagonal distribution of points mostly included in a buffer area of 1 cm, roughly representing the accuracy of the observed InSAR displacements. A
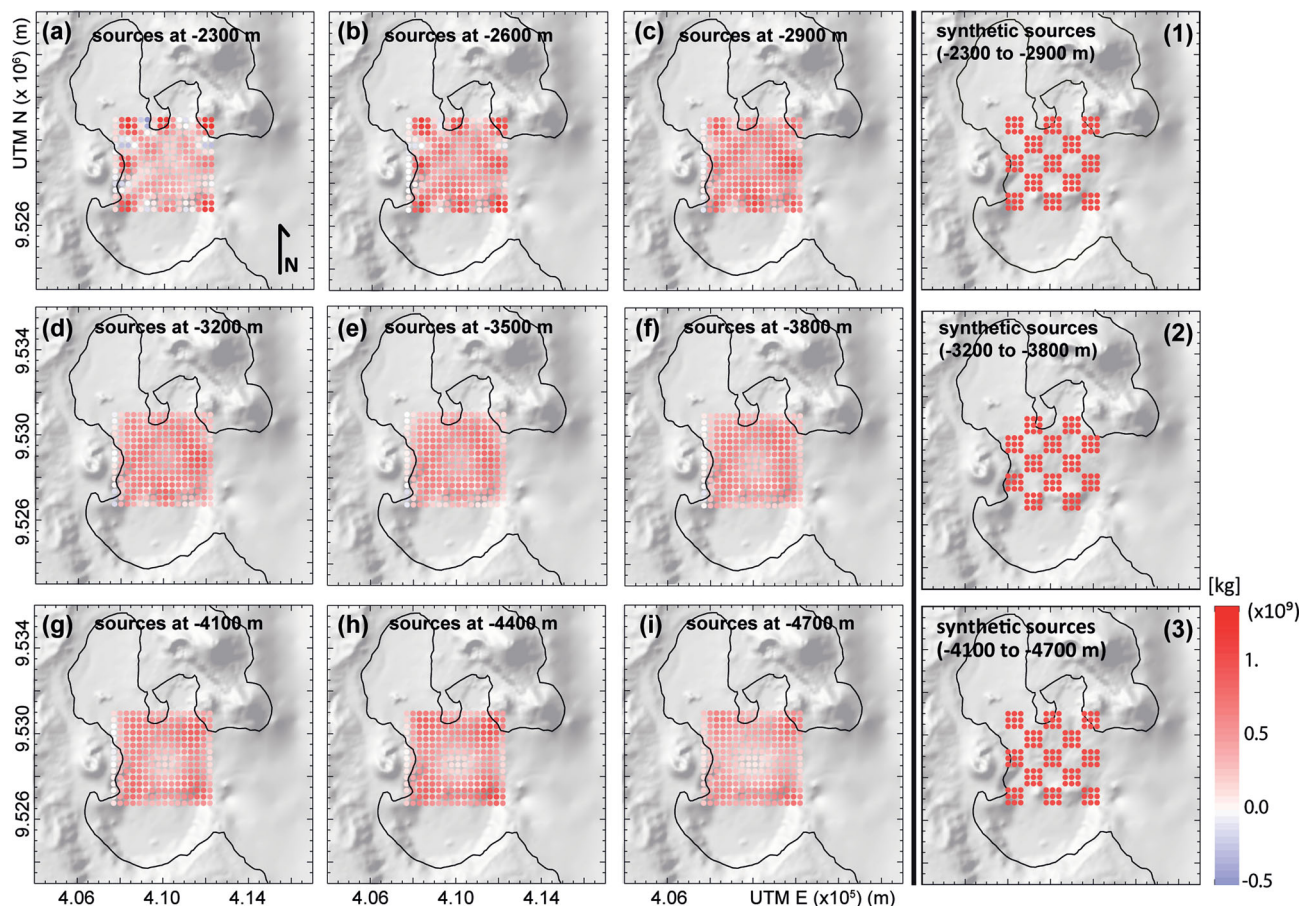
Figure 6. Checkerboard resolution test. For each row, the last panel represents the synthetic sources to be obtained through the inversion; the first three panels represent the results of the inversion. (a)–(i) Estimated sources from the checkerboard input on the right. (1)–(3) Checkerboard pattern of sources used for the resolution test.

uniform, broad, but small misfit is observed west of the caldera border. The highest misfits are recorded for the points inside the caldera and in particular for the areas north of Matupit Island (Fig. 4e).

The solutions of the WLSD inversion (Figs 5a–i) show the distribution of fluid flux (change of fluid mass per year) in the source array. The main negative fluxes of fluid (i.e. fluid flowing out of the source) are distributed along a diagonal direction between Vulcan and Tavurvur, forming a distribution with amorphous shape (Figs 5a–i). The diagonal trend of the distribution is emphasized by a diagonal cut on its southern side (red dashed line in Figs 5e–g). Higher negative flux values are localized in two areas. A first area is located in the NE of the array (SW of Tavurvur volcanic centre), starting at 2600 m and clearly visible from 2900 m depth (Fig. 5c). The flux under this area is quite consistent over all the layers in depth (Figs 5c–i), although its negative values are higher between 3500 and 4100 m depth (Figs 5e–g) and they remarkably diminish in the deeper layer. A second area of high negative flux values, slightly elongated north–south, is located at the western side of Blanche Bay in front of Vulcan (Figs 5d–h), starting at 3200 m depth (Fig. 5d). The higher negative flux values of this area are found northeast of Vulcan at 4100 m depth, in front of Vulcan North Shore (VNS; Figs 5f and g). Distributed transitional negative flux values appear to be gradually connected at depth in these areas, starting at 3200 m (Figs 5d–h), forming a 3-D distribution with amorphous shape. The highest negative flux, -0.12×10^9 kg yr^{-1}, is reached under the first area at 3800 m depth (Fig. 5f). The total magnitude of fluid

mass flowing out of the source array is -74.5×10^9 kg yr^{-1}. Values of flux vanish on the shallower and deeper layers of the source array (Figs 5a, b and i).

To investigate the model resolution, we created a synthetic distribution of unit sources in a checkerboard pattern (Figs 61–3). The checkerboard test gives an indication of how well details are resolved by the inversion. Resolution is higher at shallower levels (Figs 6a–c), but rapidly decreases at deeper levels. Squared shapes of about 1 km side length are still recognizable in the first three levels and at the sides of the fourth, while at deeper levels the resolution is lower and the elements of the synthetic source pattern are smeared. Model uncertainties (Figs 7c–g), generally reasonable with respect to the source estimates, are higher at the southeastern corner of the array.

5 DISCUSSION

For computational reasons, complex volcano deformation sources are generally interpreted through models having simplified source geometries. The strategy proposed here allows us to integrate advanced FEMs into the inversion of InSAR data for the generation of FEM-based images of volcano reservoirs. This satisfies the need for studying and interpreting volcanic reservoirs through models with more realistic 3-D source geometries and domains that honour heterogeneous distributions of material properties as indicated by
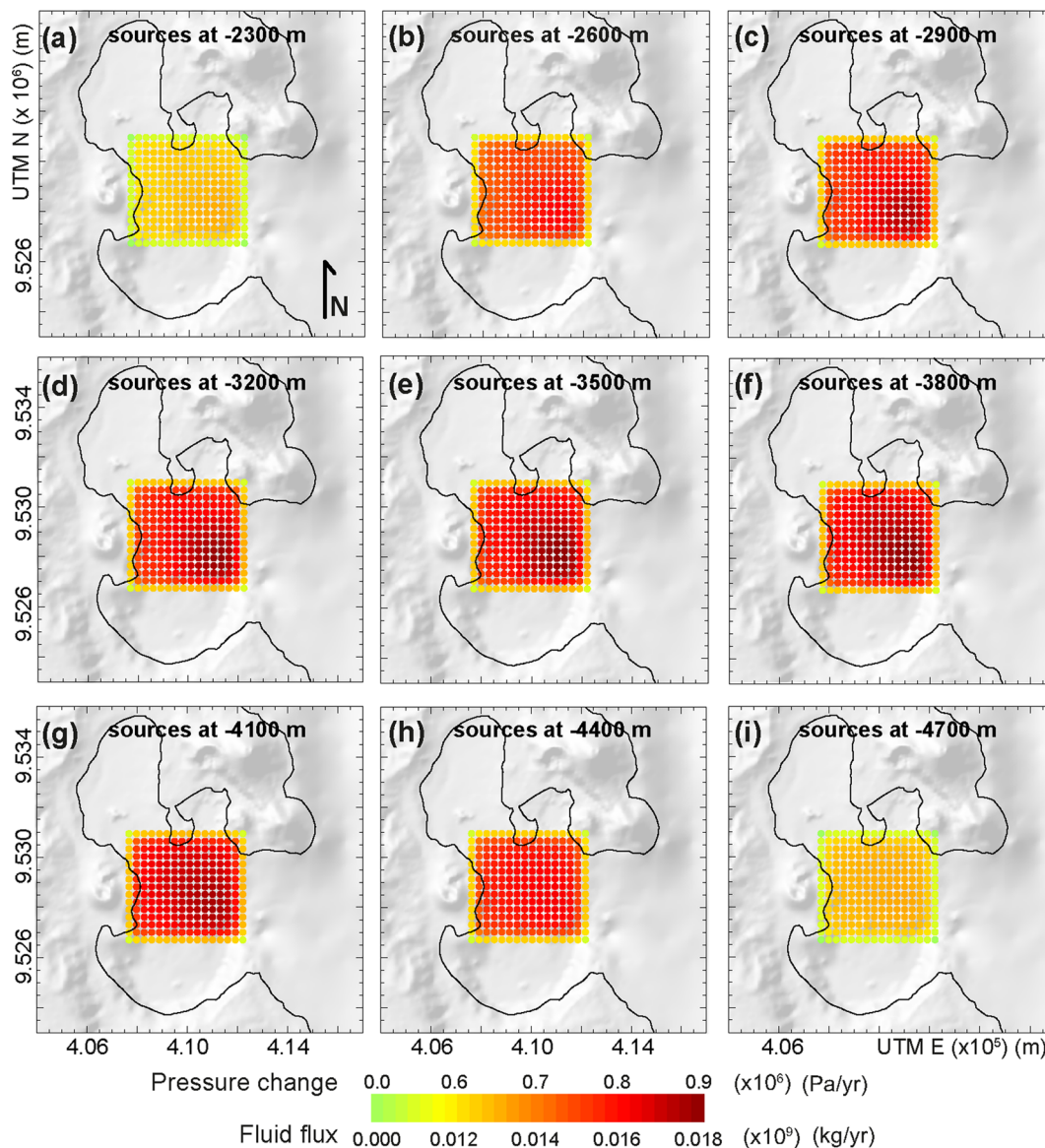
Figure 7. Model uncertainties. (a)–(i) Distribution of solution uncertainties at each level of the array of sources.

seismic tomography and geology. Results of the Rabaul case study (Fig. 5) show how the proposed strategy improves the imaging of 3-D deformation sources by identifying the location and geometry of the active parts of the reservoir. This allows tracking the evolution of reservoirs, which may thus widen the understanding of reservoir dynamics, advance our ability of monitoring active volcanoes and improve the prediction of eruptions.

The inverse solutions for a distribution of magma withdrawal (i.e. mass of fluid leaving the sources) and the related pressure change track the extension and shape of the shallow magmatic reservoir under the Rabaul caldera (Figs 5 and 8). The solutions of mass removal show a complex distribution made of two areas of high values: a first one located at the northeastern corner of the array, starting at shallower levels, merges at higher depths (between −3500 and −4400 m, in Figs 5e and f) with a second one located on the western side of the caldera, NE of Vulcan. When considering the shape of the amorphous distribution of sources as possible source of deformation, we must keep in mind the resolution of the inversion model used. In our case, the resolution of the model (Figs 6a–i)

allows us to detect the presence of two areas of higher negative flux values at the borders of the source array, starting at different depths (Figs 5c and d). For depths deeper than 3500 m (Figs 5e–i), no further details than a smeared distribution of sources at the centre of the array can be achieved due to the lower model resolution (Figs 6e–i). Thus, the inverse solution favours shallow sources at the sides of the array where the resolution of the model is higher (Figs 6a–c). Higher resolution is found near and beneath the coastline, as no deformation data are available from the bay. No data coverage over the bay, together with the way the data variance is mapped to model parameters, determines higher uncertainties for source estimates in the southeastern corner (Figs 7c–g), while smaller uncertainties correspond to source estimates at the western and northern side of the array.

Correspondences between the estimated distribution of fluid fluxes and the geological features, petrographic information and observations of the volcanic activity support our solution. The elongated distribution of fluid mass withdrawal, oriented SW-NE between Vulcan and Matupit Island and centred at about 3500 m
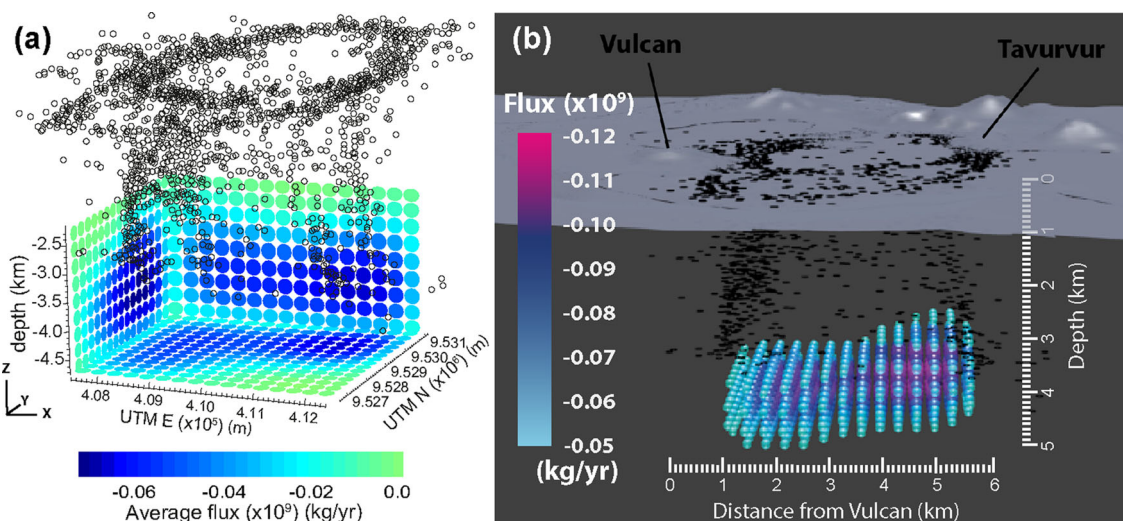
Figure 8. 3-D views of the source of deformation. (a) View of average flux values projected on three orthogonal planes. (b) Values of flux under the topography of the Rabaul caldera (view from south). For better visualization only data with values $< -0.05 \times 10^9$ kg yr^{-1} are plotted. In both panels, black circles represent the seismicity from Saunders (2001).

depth (Fig. 8a), does not laterally intersect the seismicity recorded at Rabaul caldera central elliptical faults between 1971 and early 1992 (Fig. 5). This is consistent with the assumption that the faults do not propagate in the molten rock and define a physical constraint for the reservoir. In particular, we observe that the distribution of fluid flux in all levels is confined to the shallower seismicity (<2 km depth, red dots in Fig. 5b), resembling its shape on the southeastern side (dashed red line in Figs 5e–h). This suggests a possible relationship between the extension of the imaged reservoir and the faults related to the shallower seismicity. The old submarine cones inside the caldera, located at the border of the imaged reservoir (Fig. 5a), suggest a possible correlation with the southernmost extension of the reservoir. Folds mapped during seismic reflection surveys (Pono 1990) show SW-NE trends on top of the imaged reservoir, resembling the elongation of the reservoir itself (Fig. 5a). The higher and shallower flux values, located SW of Tavurvur (Fig. 8b) and having broad vertical extension, are consistent with a higher withdrawal in this volume of the array due to the almost continuous vulcanian eruptions at Tavurvur. The western side of the amorphous distribution of sources is consistent with a batch of magma that could have fed the 1994 eruption at VNS (Fig. 5a). Furthermore, its elongated N-S shape, with slightly higher values on its northern part (Fig. 5f), resembles the distribution of historical cones (Vulcan Island, Vulcan and VNS) on the western side of the caldera (Fig. 5a).

By assuming that the observed deformation is caused by sources confined to the prism depth, we neglect: (1) the feeding dykes from below and (2) the very shallow processes having small deformation wavelength and short-period deformation impulses, such as localized hydrothermal processes or the intrusion of shallow dykes that connect the reservoir to the Tavurvur eruptive centre. The first point implies that we are modeling a half-opened system in which we assume that the mass of fluid can only flow out of the system, ignoring any new input of magma from deeper reservoirs. This assumption is a reasonable approximation based on the fact that the absence of petrographic changes in the volcanic products from the October 2006 eruption (RVO reports in Smithsonian Institution 2013) suggests that no significant replenishment of the shallow reservoir occurred during the period studied. The second point arises from the goal of focusing the investigation on the shape and extension of the

reservoir by using its long-lasting deformation signal, rather than on shallow and short-period processes, such as the feeding of local vents or the hydrothermal activity, which is still poorly understood (Johnson *et al.* 2010).

The interconnection of sources at depth (Figs 5 and 8) finds correspondence in the products erupted in 2006 October and during the study period, as well as in products erupted at Rabaul during previous eruptions (Patia 2004; Bouvet de Maisonneuve *et al.* 2015). In fact, the andesites erupted during 2006 October are the results of the mixing and mingling of two magmas from the same system at a depth calculated between 2.7 and 3.8 km: a replenishing basalt and a resident dacite (Bouvet de Maisonneuve *et al.* 2015). Less evolved magmas are erupted from Tavurvur, on the eastern side of the caldera, suggesting a more direct feeding by basaltic magmas from a deeper part of the system on this side of the caldera (Roggensack *et al.* 1996). Dacites are the only products erupted from vents on the western side of the caldera (Roggensack *et al.* 1996), thus suggesting that the western area of the reservoir imaged by the solutions could represent part of the resident dacite batch. The estimated interconnection of sources at depth suggests a possible migration and interaction of fluids from opposite sides of the reservoir, which is consistent with the mixing and mingling processes observed by other authors (Patia 2004; Bouvet de Maisonneuve *et al.* 2015).

The existence of two sources at Rabaul has been proposed by previous analytical half-space homogenous models, based on the data collected during the seismo-deformational crisis of 1983–1985: one source located southeast of Matupit Island, at a depth between 1.2 and 2 km (Fig. 5a), and another under Vulcan at a depth of 3 km (Fig. 5d; McKee *et al.* 1984, 1989; Archbold *et al.* 1988). The distribution of our solutions resembles these sources, although locating them at higher depths. Thus, our study confirms and extends the results of these early studies. Compared to the previous models, the proposed model allows a more realistic domain with heterogeneous distribution of material properties and a corresponding source geometry that is determined by the deformation data. In fact, the model depicts reservoir details unachievable by using single *a-priori* sources and features not solved at the resolution of the tomography. Moreover, it allows detecting the connection between two relatively shallow batches of magma where the mixing and mingling of the

two magmas can occur, as already hypothesized by petrographic studies (Patia 2004; Bouvet de Maisonneuve *et al.* 2015).

The estimated total amount of mass withdrawal per year is 74.5×10^9 kg yr^{-1}. This corresponds to an estimated total volume of 119×10^6 m^3, withdrawn by almost continuous Tavurvur vulcanian eruptions during the entire study period. Although we do not have independent information about the erupted volume to validate our estimate, we believe that we are proposing a reasonable value, considering that the volume of the 2006 eruption, 200×10^6 m^3 (see Saunders et al. 2007), could be a reference value for a typical eruptive volume over a short period at Rabaul.

Pressure values calculated for the sources (Fig. 5) are realistic, being smaller than the shear strength of diorite in which the sources are located. This, at first approximation, prevents a slip along fractures. In fact, no collapses that were observed during the period studied.

A little area of anomalous positive LOS velocities is observed along the southwestern side of the old airport strip, north of Matupit Island (Fig. 4e). This anomaly may reflect a local groundwater or soil compaction signal, since this is a drainage area. The small but broad misfit west of the caldera could be generated by tectonic movements or deeper sources not considered in our model.

The distribution of pressure changes, provided as variable solutions by the hydrostatic elements (Abaqus 2009), is valuable information for studies whose aim is the understanding of the magmatic processes occurring inside a reservoir, which generate pressure changes responsible for surface deformations. In this work, a principal assumption is that the change of magma mass, which changes both the pressure and volume of a given source, is entirely due to a magma mass flux into or out of the system. It is important to note, however, that alternative mechanisms could be responsible for the pressure and volume variation (e.g. crystallization, degassing, remelting, expansion of the hydrothermal system, etc.) that may have different relationship with the change of mass in the system. In further studies, with gravity data available, the gravity signal could be modeled and a fully joint inversion of gravity and deformation could be performed in order to discriminate the processes responsible for the deformation. Therefore, we believe that the proposed model, by simulating change of mass, pressure, volume and deformation, could open up further studies combining deformation and microgravity data that could better shed light on the mechanisms responsible for surface displacements at active volcanoes.

6 CONCLUSIONS

In this work, we propose a computationally inexpensive strategy for an FEM-based linear inversion of InSAR data capable of estimating the extended, arbitrary distribution of mass and pressure changes within the integration domain of FEM models. This method leads to the creation of 3-D images of the sources responsible for surface deformation. The method pushes FEM-based inverse modeling a step forward by removing the requirement for *a-priori* assumptions regarding the shape of volcano deformation sources and letting the data dictate the shape of the deformation source as a spatial distribution of mass flux, and thus a distribution of pressurization throughout a geometrically complicated reservoir.

By applying the method to InSAR data of Rabaul caldera, we have been able to image the extent and shape of the active reservoir (Fig. 8b). Our study images the presence of two main sources at opposite sides of the caldera and connected at depth,

showing that the shallow magmatic system is an interconnected reservoir instead of distinct magma bodies. This implies a high mobility of magma between different parts of the system and explains how a long-lasting eruption at one side of the caldera, in this case at Tavuvur, can trigger a long-term deflation of the entire system.

REFERENCES

Abaqus, 2009. Version 6.9-EF, Dassault Systèmes Simulia Corp., Providence, RI. Available at: www.simulia.com, last accessed August 2014.

Archbold, M.J., McKee, C.O., Talai, B., Mori, J. & De Saint Ours, P., 1988. Electronic distance measuring network monitoring during the Rabaul seismicity/deformational crisis of 1983–1985, *J. geophys. Res.,* **93,** 12 123–12 136.

Aster, R.C., Borchers, B. & Thurber, C.H., 2005. *Parameter Estimation and Inverse Problems*, pp. 360, 2nd edn., Elsevier Academic Press, Boston.

Battaglia, M. & Vasco, D., 2006. The search for magma reservoirs in Long Valley caldera: single vs. distributed sources, in *Mechanisms of Activity and Unrest at Large Calderas*, Vol. 269, pp. 173–180, eds Troise, C., De Natale, G. & Kilburn, C.R.J. Geological Society of London, Special Publication.

Bouvet de Maisonneuve, C, Costa, F., Patia, H. & Huber, C., 2015. Unrest and eruption in a caldera setting: insights from the 2006 eruption of Rabaul (Papua New Guinea), *Geol. Soc. Lond., Spec. Publ.,* **422**(1), 17–39.

Burchardt, S., Tanner, D.C. & Krumbholz, M., 2010. Mode of emplacement of the Slaufrudalur Pluton, Southeast Iceland inferred from three-dimensional GPS mapping and model building, *Tectonophysics,* **480**(1–4), 232–240.

Burchardt, S., Troll, V.R., Mathieu, L., Emeleus, H.C. & Donaldson, C.H., 2013. Ardnamurchan 3D cone-sheet architecture explained by a single elongate magma chamber, *Sci. Rep.,* **3,** 2891, doi:10.1038/srep02891.

Camacho, A.G., Fernández, J., Charco, M., Tiampo, K.F. & Jentzsch, G., 2007. Interpretation of 1992–1994 gravity changes around Mayon Volcano, Philippines, using point sources, *Pure appl. Geophys.,* **164,** 733–749.

Camacho, A.G., González, P.J., Fernández, J. & Berrino, G., 2011. Simultaneous inversion of surface deformation and gravity changes by means of extended bodies with a free geometry: application to deforming calderas, *J. geophys. Res.,* **116,** B10401, doi:10.1029/2010JB008165.

De Natale, G. & Pingue, F., 1993. Ground deformations in collapsed caldera structures, *J. Volc. Geotherm. Res.,* **57,** 19–38.

De Natale, G., Petrazzuoli, S.M. & Pingue, F., 1997. The effect of collapse structures on ground deformations in calderas, *Geophys. Res. Lett.,* **24,** 1555–1558.

Farr, T.G. *et al.*, 2007. The shuttle radar topography mission, *Rev. Geophys.,* **45,** 1–43.

Fernández, J., Tiampo, K.F. & Rundle, J.B., 2001. Viscoelastic displacement and gravity changes due to point magmatic intrusions in a gravitational layered solid earth, *Geophys. J. Int.,* **146,** 155–170.

Finlayson, D.M., Gudmundsson, O., Itikarai, I., Nishimura, Y. & Shimamura, H., 2003. Rabaul volcano, Papua New Guinea: seismic tomographic imaging of an active caldera, *J. Volc. Geotherm. Res.,* **124,** 153–171.

Freymueller, J., King, N.E. & Segall, P., 1994. The co-seismic slip distribution of the Landers earthquake, *Bull. seism. Soc. Am.,* **84,** 646–659.

Got, J.-L., Monteiller, V., Monteux, J., Hassani, R. & Okubo, P., 2008. Deformation and rupture of the oceanic crust may control growth of Hawaiian volcanoes, *Nature,* **451,** 453–456.

Hickey, J., Gottsmann, J. & Mothes, P., 2015. Estimating volcanic deformation source parameters with a finite element inversion: the 2001–2002 unrest at Cotopaxi volcano, Ecuador, *J. geophys. Res.,* **120**(B011731), 126–130.

Hooper, A. & Zebker, H.A., 2007. Phase unwrapping in three dimensions with application to InSAR time series, *J. Opt. Soc. Am.,* **24,** 2737–2747.

Hooper, A., Segall, P. & Zebker, H., 2007. Persistent scatterer interferometric synthetic aperture radar for crustal deformation analysis, with application to Volcán Alcedo, Galápagos, *J. geophys. Res.,* **112,** 1–21.

Huang, H.H., Lin, F.C., Schmandt, B., Farrell, J., Smith, R.B. & Tsai, V.C., 2015. The Yellowstone magmatic system from the mantle plume to the upper crust, *Science,* **348,** doi:10.1126/science.aaa5648.

Huppert, H.E. & Woods, A.W., 2002. The role of volatiles in magma chamber dynamics, *Nature,* **420**(6915), 493–495.

Jaxybulatov, K., Shapiro, N.M., Koulakov, I., Mordret, A., Landes, M. & Sens-Schonfelder, C., 2014. A large magmatic sill complex beneath the Toba caldera, *Science,* **346**(6209), 617–619.

Johnson, R.W., Itikarai, I., Patia, H. & McKee, C.O., 2010. Volcanic systems of the Northeastern Gazelle Peninsula, Papua New Guinea: synopsis, evaluation, and a model for Rabaul Volcano, Papua New Guinea, Rabaul Volcano Workshop Rep., Papua New Guinea Department of Mineral Policy and Geohazards Management, Port Moresby, Papua New Guinea.

Jones, R.H. & Stewart, R.C., 1997. A method for determining significant structures in a cloud of earthquakes, *J. geophys. Res.,* **102,** 8245–8254.

Lohman, R.B. & Simons, M., 2005. Some thoughts on the use of InSAR data to constrain models of surface deformation: noise structure and data downsampling, *Geochem. Geophys. Geosyst.,* **6,** Q01007, doi:10.1029/2004GC000841.

Massonnet, D. & Feigl, K.L., 1998. Radar interferometry and its application to changes in the Earth's surface, *Rev. Geophys.,* **36,** 441–500.

Masterlark, T. & Lu, Z., 2004. Transient volcano deformation sources imaged with interferometric synthetic aperture radar: application to Seguam Island, Alaska, *J. geophys. Res.,* **109,** B01401, doi:10.1029/2003JB002568.

McKee, C., Mori, J. & Talai, B., 1989. Microgravity changes and ground deformation at Rabaul caldera, 1973–1985, in *IAVCEI Proceedings in Volcanology,* pp. 399–431, ed. Latter, J. Springer, Berlin.

McKee, C.O., Lowenstein, P.L., de Saint Ours, P., Talai, B., Itikarai, I. & Mori, J.J., 1984. Seismic and ground deformation crises at Rabaul Caldera: prelude to an eruption?, *Bull. Volcanol.,* **47,** 397–411.

McTigue, D.F., 1987. Elastic stress and deformation near a finite spherical magma body: resolution of the point source paradox, *J. geophys. Res.,* **92,** 12 931–12 940.

Menke, W., 1989. *Geophysical Data Analysis: Discrete Inverse Theory,* International Geophysics Series, Vol. 45, 1st edn, Academic Press, San Diego.

Minasny, B., McBratney, A.B. & Walvoort, D.J.J., 2007. The variance quadtree algorithm: use for spatial sampling design, *Comput. Geosci.,* **33,** 383–392.

Mori, J. & McKee, C.O., 1987. Outward-dipping ring-fault structure at Rabaul caldera as shown by earthquake locations, *Science,* **235,** 193–195.

Mossop, A. & Segall, P., 1999. Volume strain within The Geysers geothermal field, *J. geophys. Res.,* **104,** 29 113–29 131.

Patia, H., 2004. Petrology and geochemistry of the recent eruption history at Rabaul Caldera, Papua New Guinea: implications for magmatic processes and recurring volcanic activity, *PhM thesis,* University of Papua New Guinea, Port Moresby.

Pono, S., 1990. Caldera structures of Rabaul harbour from seismic reflection profiles, SOPAC, Tech. Rep. 87, Geological Survey of Papua New Guinea, Port Moresby.

Roggensack, K., Williams, S.N., Schaefer, S.J. & Parnell, R.A., Jr, 1996. Volatiles from the 1984 Eruptions of Rabaul: understanding Large Caldera Systems, *Science,* **273,** 490–493.

Ronchin, E., Masterlark, T., Martí, J., Saunders, S. & Tao, W., 2013. Solid modeling techniques to build 3D finite element models of volcanic systems: an example from the Rabaul Caldera system, Papua New Guinea, *Comput. Geosci.,* **52,** 325–333.

Rosen, P.A., Hensley, S., Peltzer, G. & Simons, M., 2004. Updated repeat orbit interferometry package released, *EOS, Trans. Am. geophys. Un.,* **85,** 47–47.

Samet, H., 1990. *The Design and Analysis of Spatial Data Structures,* 1st edn, Addision Wesley Publishing Company, Inc.

Saunders, S.J., 2001. The shallow plumbing system of Rabaul caldera: a partially intruded ring fault?, *Bull. Volcanol.,* **63,** 406–420.

Saunders, S.J., Patia, H., Taranu, F., Kuduon, J., Cowlyn, J. & Nishimura, Y., 2007. How to deal with unpredictable volcanoes in a developing country?, in *Cities on Volcanoes Conference Abstracts,* 21a-O-15, p. 112, Volcanological Society of Japan, Shimabara, Japan, 19–23 November.

Simmons, G. & Brace, W.F., 1965. Comparison of static and dynamic measurements of compressibility of rock, *J. geophys. Res.,* **70**(22), 5649–5656.

Smith, R.B. *et al.,* 2009. Geodynamics of the Yellowstone hotspot and mantle plume: seismic and GPS imaging, kinematics, and mantle flow, *J. Volc. Geotherm. Res.,* **188**(1–3), 26–56.

Smithsonian Institution, 2013. Global Volcanism Program (GVP) report for Rabaul. Available at: http://volcano.si.edu/volcano.cfm?vn=252140, last accessed November 2013.

Trasatti, E., Giunchi, C. & Bonafede, M., 2003. Effects of topography and rheological layering on ground deformation in volcanic regions, *J. Volc. Geotherm. Res.,* **122,** 89–110.

Turcotte, D.L. & Schubert, G.J., 2002. *Geodynamics: Applications of Continuum Physics to Geological Problems,* 2nd ed., Cambridge Univ. Press.

Vasco, D.W., Wicks, C., Karasaki, K. & Marques, O., 2002. Geodetic imaging: reservoir monitoring using satellite interferometry, *Geophys. J. Int.,* **149,** 555–571.

Trasatti, E., Giunchi, C. & Agostinetti, N.P., 2008. Numerical inversion of deformation caused by pressure sources: application to Mount Etna (Italy), *Geophys. J. Int.,* **172,** 873–884.

Wang, H.F. & Anderson, M.P., 1982. *Introduction to Groundwater Modeling: Finite Differences and Finite Element Methods,* 1st edn, Academic Press.

SUPPORTING INFORMATION

Supplementary data are available at *GJIRAS* online.

Figure S1. Test of cubic sources, comparison between analytical and numerical solutions. (a) Boundary conditions of the FEM model domain. (b) Details of the central prism part that hosts the cubic sources. Discretizations into cubic hexahedral elements of 500 m side (thick lines) and 250 m side (thin lines) are overlapped for convenience. Position and size of different tested sources are also illustrated (cubes in different colours). (c) Surface displacements generated by the pressurized FEM sources (dots) and the McTigue isotropic expansion sources (solid lines; McTigue 1987). Details of cavity discretization of each tested source are shown: cavity types L1 and S1 made by removing one element, cavity type L8 and L8i made by removing eight elements (colours as in panel b for location reference).

Figure S2. Array of cubic sources and test of cubic sources. (a) Boundary conditions of the FEM model domain. (b) Details of the central prism partitioned with an array of 500 m size cubic hexahedral elements. Cubic cavities of source L1, made of one single cubic hexahedral element of 500 m size (light blue) at the corner, along the edge, on the side, and at the bottom of the array

are illustrated. (c) Expansion source, pressure applied to the inner faces of the cubic cavity. (d) Details of the array of 250 m size hexahedral elements and sources at different positions in the central prism. Cubic cavities of source S1 (dark blue) and cubic cavities of source type L8 (pink) and L8i (orange) are illustrated at the corner, the edge, the upper face and the bottom face of the central prism. (e)–(h) Surface displacements generated by the tested pressurized FEM sources (dots) at the four locations inside the array and the corresponding McTigue isotropic expansion sources (solid lines). The colours of the solutions correspond to the colours used in panels (b) and (d) to highlight the cubic cavities at their position inside the central prism.

Figure S3. Time-series of PS LOS differential movement at Rabaul area. (a) Each image shows LOS displacements since the first image, acquired 2007 February 27. The LOS displacements are shown by colours as defined in the colour bar in panel (b). The scene used for the master image was acquired 2009 March 4 (black frame). (b) Total displacement over the entire period. (c) LOS displacement sign convention. (d) Interpretation of LOS displacements in the Rabaul area due to subsidence. Filled and empty pixels show the position of the terrain points over the undeformed and deformed surface, respectively. Grey arrows show the movement of the pixels; blue and red arrows represent the negative and positive movements' projections along the LOS of the satellite, respectively.

Figure S4. Testing the inversion process: inversion results for a synthetic deformation. (a) Estimation of the model source strengths. The L-curve gives the trade-off between misfit (RMSE) and model roughness. The preferred solution is obtained for the value of beta at the knee of the L-curve (red dot). (b) Synthetic versus predicted LOS displacements. The diagonal red line shows the line of perfect correspondence between synthetic and predicted solutions. (c) Synthetic LOS displacements. (d) Predicted LOS displacements. (e) Residuals between predicted and synthetic LOS displacements. (f)–(p) Solutions of the FEM-based inversion at different depths. The solutions represent the flux of fluid at each source of the source array. The 27 sources used to generate the synthetic deformation are highlighted with a black box. Red colours represent a positive flux which means that a mass of fluid is entering the source.

Table S1. Elastic formulae, size and elastic properties of the 3-D geological bodies.

Table S2. Values of parameters used to calculate the bulk modulus of Rabaul magma.

Please note: Oxford University Press is not responsible for the content or functionality of any supporting materials supplied by the authors. Any queries (other than missing material) should be directed to the corresponding author for the paper.